Acoustics of Transonic Blade-Vortex Interactions

A. R. George* and A. S. Lyrintzis†
Cornell University, Ithaca, New York

A study is made of midfield and far-field noise generated by transonic blade-vortex interactions (BVI), typical of helicopter main rotor noise. The VTRAN2 small disturbance, two-dimensional, transonic-flow code that includes convected vorticity was used to compute near-field and midfield flowfield information. Because of mesh size limitations, this information is restricted to the midfield and does not give the desired far-field and three-dimensional information. A method of extending the solutions to the far-field in three dimensions is developed based on Kirchhoff's solution to the linear flow outside a surface S enclosing the nonlinear near field. A spherical wave is first used as a test case for the method. The relation of unsteady-type "C" shock motion on the airfoil to far-field sound is shown. The far-field radiation is affected by Mach number, airfoil thickness, shape, and vortex miss distance.

Introduction

AMONG the several types of helicopter noise,[1] that due to blade-vortex interactions (BVI) is one of the most important. It is loud, impulsive in character, and tends to dominate other sources when it occurs.

BVI noise is caused by unsteady flow changes around various rotor blades due to interactions with vortices previously shed by the blades. For example, the tail rotor of a helicopter can ingest the shed vortices of the main rotor and become an important noise source.[2] However, when it occurs, probably the most important kind of BVI noise from single main-rotor helicopters is due to interactions of the main rotor with parts of its own vortex wake. As discussed in Refs. 3–5 and sketched in Fig. 1, during forward flight the tip vortices of rotor blades can interact with portions of rotor blades at various angles and miss distances. The distortion of the shed wake and the vortex core geometry are very important in determining the parameters of these BVI's.

Interactions generate the most significant noise when the vortex is exactly parallel to the blade, or when the vortex is nearly parallel to the blade. It was shown in Refs. 3 and 4 that the aerodynamics and aeroacoustics of the interactions are intrinsically transonic for typical helicopter cases. In such cases, the flow can be initially modeled by two-dimensional unsteady transonic flow, as sketched in Fig. 2.

The present research deals with the analysis of the noise generated by the resulting radiation of waves to the midfield and far-field. Two-dimensional transonic BVI was first studied computationally in the near field and midfield by George and Chang,[3,4] who used the transonic small-disturbance theory, including regions of convected vorticity. References 3 and 4 contain detailed discussions of the background and formulation of the transonic BVI problem. McCroskey and Goorjian,[6] Srinivasan et al.,[7] and Baeder et al.[8] also solved the two-dimensional problem with the small-disturbance theory and with the more complex Euler and thin-layer Navier-Stokes equations. Recently, Baeder et al.[8] presented some near-field and midfield results that will be discussed in relation to the present results. In Ref. 9, some midfield results were presented and also, for the first time, a Kirchhoff method of extending the computed two-dimensional midfield results to the three-dimensional far-field was introduced. More results with some three-dimensional calculations were also shown in Ref. 10.

Presented as Paper 86-1854 at the 10th AIAA Aeroacoustics Conference, Seattle, WA, July 9–11, 1986; received March 16, 1987; revision received Nov. 16, 1987.

*Professor, Sibley School of Mechanical and Aerospace Engineering. Associate Fellow AIAA.

†Graduate Research Assistant, Sibley School of Mechanical and Aerospace Engineering; currently, Assistant Professor, Mechanical and Aerospace Engineering Department, Syracuse University, Syracuse, NY. Student Member AIAA.

Numerical Method (VTRAN2)

VTRAN2 is a transonic small-disturbance theory code[3,4] developed for analyzing the interactions of convected regions of vorticity with airfoils. It is based on the LTRAN2 low-frequency transonic small-disturbance code[11] with the additional capability of including regions of convected vorticity and the full unsteady, small-disturbance formulation.

The equation for the unsteady, inviscid, transonic small-disturbance potential is

$$A\phi_{tt} + 2B\phi_{xt} = C\phi_{xx} + \phi_{yy} \tag{1}$$

where $A = k^2M^2/\delta^{2/3}$, $B = kM^2/\delta^{2/3}$, and $C = (1 - M^2)/\delta^{2/3} - (\gamma + 1)M^m\phi_x$, and where ϕ is the disturbance-velocity potential, M is the freestream Mach number, δ is the airfoil thickness ratio, k is the reduced frequency $\omega c/U_o$, U_o is the freestream velocity, and ω is the characteristic frequency of the unsteady motion. The characteristic frequency of the motion depends on how close laterally the disturbing vortex passes to the airfoil. For large miss distances y_v (see Fig. 2), the characteristic frequency ω is U_o/y_v and thus $k = c/y_v \ll 1$; thus, the k^2 term in A implies that the first term in Eq. (1) can be dropped giving the low-frequency small-disturbance theory. However, for BVI cases of interest $y_v \leq c$, one expects

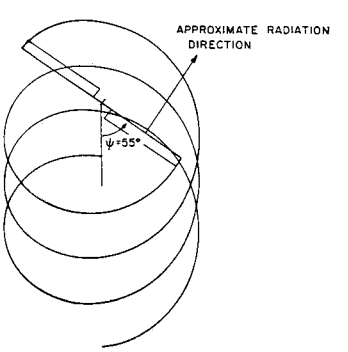

Fig. 1 Schematic view of nearly parallel interaction of advancing helicopter blade with tip vortex.

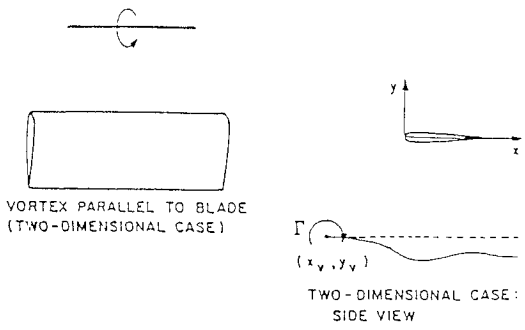

Fig. 2 Two-dimensional blade-vortex interaction geometry.

$\omega \approx U_o/c$ and thus $k \approx 1$ and the full small-disturbance theory of Eq. (1) is needed. The quantities x, y, t, and ϕ in Eq. (1) have been scaled by c, $c/\delta^{1/3}$, ω^{-1}, and $c\delta^{2/3}\ U_o$, respectively. Since time t is nondimensionalized, the choise of k is irrelevant and was taken as $k = 1$ ($\omega = U_o/c$), meaning that one time unit corresponds to a freestream convection of one chord length. The exponent m in the nonlinear term is chosen as $m = 2$, which is suitable for stronger shocks since it locates the shocks more accurately.[11]

The boundary conditions in the computational plane are shown in Fig. 3. They inlcude

Upstream outer boundary condition:

$$\phi_x = \phi_y = 0 \qquad \text{as } x \to \infty$$

Lateral outer boundary condition:

$$\phi_x = \phi_y = 0 \qquad \text{as } y \to \pm\infty$$

Downstream outer boundary condition:

$$\phi_x + k\phi_t = 0 \qquad \text{as } x \to +\infty$$

Airfoil surface boundary condition:

$$\phi_y = \partial Y_\pm/\partial x + k\partial Y_\pm/\partial t$$

where $Y_\pm$ defines the airfoil surface.

In addition, the wake condition $\Gamma_x + k\Gamma_t = 0$ implies that a branch cut exists between the trailing edge and the downstream outer boundary, across which the potential jump $\Delta\phi = \Gamma$, where Γ is the airfoil circulation. Also, several branch cuts with potential jumps due to the distributed moving vortex must be introduced along y = constant grid lines.[3,4] The vortex can have a free path (convected by the flow) or a prescribed path (y_o = constant, vortex velocity = U_o).

The pressure coefficient C_p in the unsteady small-disturbance theory is

$$C_p = -2(\phi_x + k\phi_t)$$

The VTRAN2 code uses the ADI implicit scheme of LTRAN2[12] with the addition of the ϕ_{tt} term following Rizzetta and Chin[13] and the addition of convected vorticity using the cloud-in-cell and multiple branch-cut approach.[3,4]

A fine 213×119 mesh is used for the calculations. The computational mesh points are clustered more densely near and in front of the airfoil (see Fig. 4) and then are stretched exponentially from the near airfoil region to about 200 chord lengths from the airfoil in both x and y directions. We should also note that although the outer boundary conditions used are reflective, the large computational region used (-200, 200 chords) insures that the reflections from the boundaries are very small by the time they arrive back in the region near the airfoil, and, in any case, they arrive much later than the time of interest here.

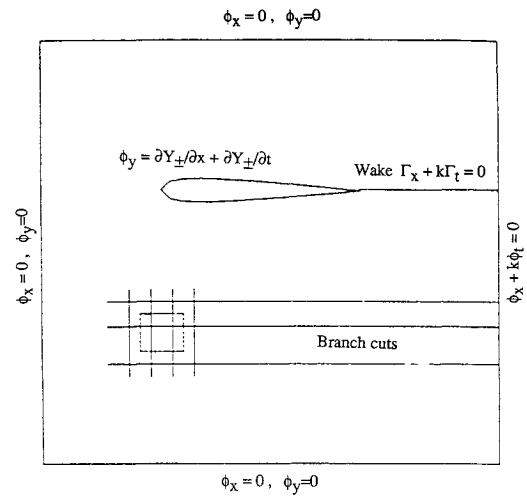

Fig. 3 Boundary conditions and region of vorticity in VTRAN2 formulation (not to scale).

The VTRAN2 code was shown to agree well with other, more complex approaches including Euler and thin-layer Navier-Stokes computations.[4] VTRAN2 can be used for calculations of the effects of airfoil shape, angle of attack, Mach number, vortex strength, and vortex miss distance on the flow and on the radiated sound. The CPU time on an IBM 4381 is between 20 and 30 min for each two-dimensional case for a fine mesh 213×119 and 500 time-marching steps.

Midfield Results

Initially, some midfield calculations were performed using VTRAN2 with a refined mesh to follow the waves of interest. Since the stronger waves propagate primarily upstream, more mesh points were added in the x direction in front of the airfoil. It is also well known[14] that in the far-field, near-wave fronts, the amplitude of two-dimensional propagating waves is proportional to $1/r^{1/2}$; thus, in order to identify the waves better, the steady-state solution with the vortex far upstream was subtracted, and the result was multiplied by $r^{1/2}$. Using this technique the wave can be clearly identified as far as two chord lengths in front of the airfoil.

At larger distances, where the computational mesh becomes coarser, the numerically calculated waves become considerably smeared and dispersed. In fact, the actual distance the wave has propagated relative to the fluid is much bigger than the two chord lengths relative to the airfoil. This is because, for M not equal to zero, any wave front propagates normal to its front, relative to the fluid, at the speed of sound c_o but is swept in the x direction with the velocity of the fluid Mc_o as shown in Fig. 5a. As a result, the geometric center of a disturbance is located at a point convected downstream at the velocity of the fluid Mc_o, as also shown in Fig. 5a.

Thus, there are two ways of looking at the waves produced by BVI. The first way[3,4] is to assume that some part of the airfoil is the source of the noise as shown in Fig. 5b. The wave fronts are viewed as originating from the airfoil as the vortex convects by. Each disturbance propagates in the moving fluid. Then, if a second disturbance originates at a second time from the airfoil, its convected disturbance center will be different from that of the first disturbance. In coordinates relative to the airfoil, its wave front propagates similarly to that of the first disturbance, as shown in Fig. 5b. Thus, it is natural to plot $c_p(t)$ for points fixed with respect to the airfoil.

The second way[8] is to assume that disturbances are always emitted at the vortex location, i.e., that the center of any disturbance is always the x position of the vortex as shown in

Fig. 5c. This point of view leads to considering coordinates fixed with respect to the fluid with the airfoil moving. The initial flowfield without a vortex must be subtracted in this case as the basic steady flowfield of the airfoil is swept over the observation point.

Before we proceed comparing the two methods, we shall define the three basic types of unsteady shock motion that were introduced by Tijdeman:[15] 1) type "A" shock motion, where the shock at the rear of the supersonic region merely moves back and forth with concurrent changes in strength; 2) type "B" shock motion, where the shock moves similarly to type "A" but disappears temporarily during the unsteady motion; 3) type "C" shock motion, where the supersonic region disappears and a shock wave leaves the airfoil and propagates forward to the far field. The existence of type "C" shock motion is BVI was verified experimentally by Tangler[16] and Caradonna et al.[17]

Both ways of looking at the waves produced by BVI are effective in following the noise produced when the vortex meets the leading edge of the airfoil, and in principle all their results can be transformed into each other. However, the second, fluid-fixed way is not as effective in following any waves that originate at the airfoil when the vortex has been convected a chord length or more behind the airfoil. Such waves typically are associated with unsteady shock motion on the airfoil, notably type "C" shock motion which typically

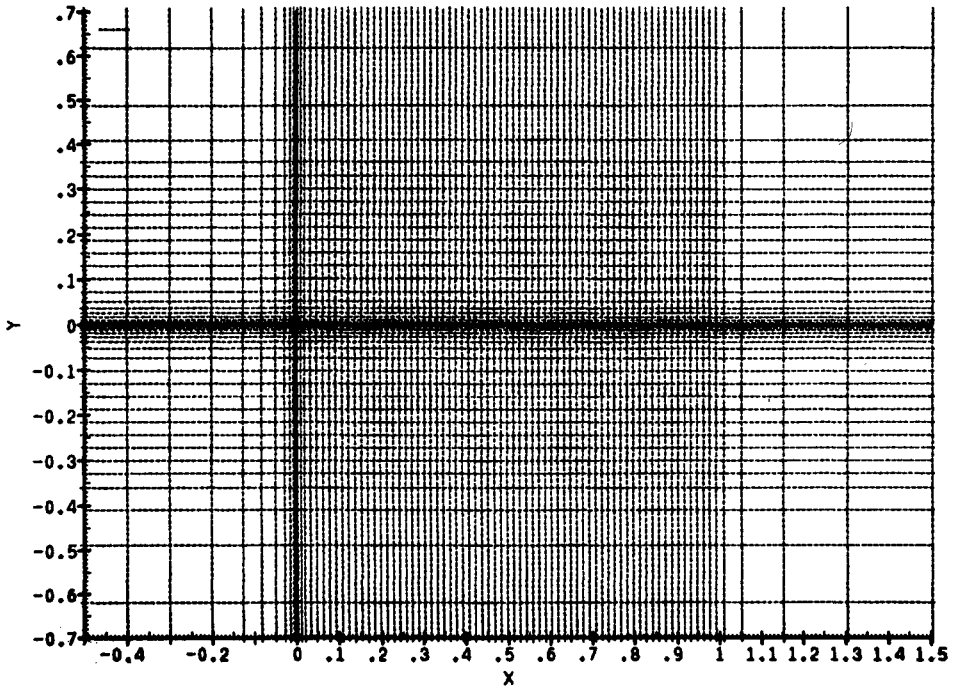

Fig. 4 VTRAN2 computational mesh distribution in near field and midfield; for clarity only every other line is shown.

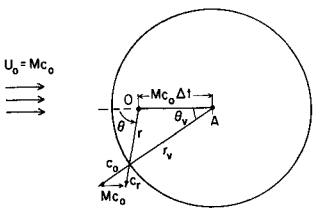

Fig. 5a Propagation and convection of a wave from a point disturbance in a flow with a freestream velocity $U_o = Mc_o$: O = disturbance origin; A = convected center of disturbance wave; c_r = ray velocity.

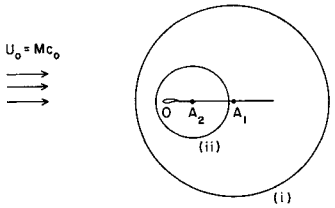

Fig. 5b Initial (i) and subsequent (ii) disturbances originating from airfoil in a flow with freestream velocity $U_o = Mc_o$; A_1 and A_2 are the convected centers of disturbances.

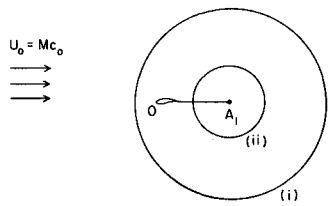

Fig. 5c Initial (i) and subsequent (ii) disturbances originating from a convected vortex in a flow past an airfoil.

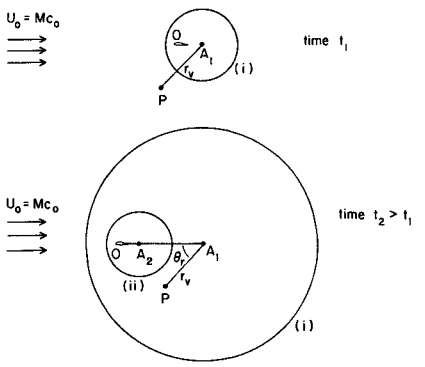

Fig. 5d Initial (i) and subsequent (ii) disturbances originating from airfoil viewed from a point P in fluid-fixed coordinates.

originates from an unsteady shock escaping from the airfoil when the vortex is 5 to 6 chord lengths behind the airfoil.[3,4] The vortex-oriented, or fluid-fixed, viewpoint is closer to the case of a helicopter flyover, except that forward-radiated disturbances in the midfield which are emitted at times after the vortex passage are difficult to observe. This is illustrated in Fig. 5d where the observer at point "P" will only observe the rearward-going part of the second disturbance.

Baeder et al.[8] used a heavily clustered grid in the leading edge region where he expected to find the biggest influence from the interaction. Hence, Baeder's results could not be expected to find waves behind the airfoil due to the way the solution was generated. In our computations, when we used the fluid-fixed approach, we had difficulty in numerically defining the second wave, which was easily visible in our airfoil-fixed approach. The wind tunnel and in-flight-observer experiments of Schmitz and Yu[5] are an intermediate case where both the fluid and the airfoil move relative to the observer.

The time history of the pressure coefficient $C_p(t)$ was studied using VTRAN2 for the ray of points in airfoil-fixed coordinates shown in Fig. 6 at an angle θ around 30 deg below the horizontal. In Fig. 7, the scaled $c_p(t)$ distributions are plotted for a NACA 64A006 airfoil, Mach number 0.822, vortex strength $c_{lv} = 0.4$, (c_{lv} is a nondimensional expression of the vortex strength: the lift that an airfoil of the same circulation as the vortex would have: $2\Gamma/U_o c$), miss distance $y_o = -0.50$, zero angle of attack, and prescribed vortex path ($y_v = y_o, dx_v/dt = U_o$). For this case, which is related to type "C" shock motion, two waves can be detected propagating to the midfield (labeled I, II). Disturbance I is the main BVI noise and originates at the airfoil when the vortex meets it. Disturbance II was shown to correspond to the type "C" shock motion and originates at the airfoil at a later time. The existence of a second pulse because of the type "C" shock motion was also verified experimentally by Caradonna et al.[17] and numerically by Owen and Shenoy.[18] It is also interesting to note that there is a fairly large initial disturbance (labeled III) when the vortex first approaches the airfoil, the bulk of which does not seem to propagate. It is related to the vortex passage near the points where the $c_p(t)$ is located.

We see from Fig. 7 that, when they are scaled, both disturbances I and II increase for points 1, 2, and 3, indicating that the two-dimensional far-field has not yet been reached. For the farther points 4, 5, and 6, we see that the amplitude of the scaled disturbances I and II approach a constant. This behavior is expected, because the $1/r^{1/2}$ rule applies only to the two-dimensional, linear far-field, called the midfield in this paper. The time lags of the moving disturbances can be shown to correspond to propagation with the speed of sound relative to the fluid as shown in Fig. 5a.

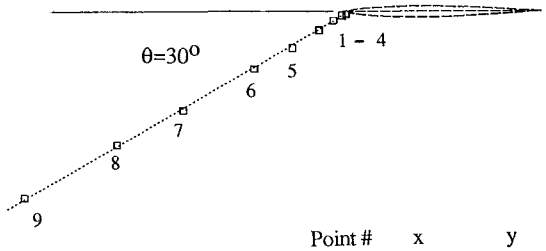

Point #	x	y
1	-0.015	-0.013
2	-0.037	-0.020
3	-0.082	-0.045
4	-0.158	-0.095
5	-0.300	-0.188
6	-0.500	-0.297
7	-0.870	-0.515
8	-1.219	-0.696
9	-1.704	-0.977

Fig. 6 Identification of one ray of points where $c_p(t)$ was calculated.

At further distances, the waves are difficult to follow numerically. This numerical method is limited by the mesh size and the time step and only allows the following of the strongest waves generated by the interaction. A finer mesh (229 × 119) with extra points in the x direction just in front of the airfoil was also used, without improving the results significantly. Also in Ref. 8, a very fine mesh (399 × 195) was used without managing to go farther than 10 chord lengths propagation relative to the fluid, which was also achieved by our coarser mesh but with less accuracy. The results are interesting but a more accurate method is needed for the far-field radiation and to be able to look at three-dimensional effects.

Kirchhoff's Method for the Midfield and the Far-Field

In order to obtain better understanding of the midfield and the far-field radiation, Kirchhoff's method is used. This method uses a Green's function for the linearized governing equation to derive a representation for the solution in terms of its values and derivatives on a closed surface S in space, which is assumed to include all the nonlinear flow effects and noise sources. A full three-dimensional formulation is used, because the Green's function is simpler in this case, and because the method can be easily extended to include spanwise variations to model three-dimensional BVI.

The Green's function G for the linear, unsteady potential flow is the solution of the equation

$$\nabla^2 G - \left(\frac{1}{c_o^2}\right)\left(U_o \frac{\partial}{\partial x} + \frac{\partial}{\partial t}\right)^2 G = \delta(x - x_1, y - y_1, z - z_1, t - t_1) \tag{2}$$

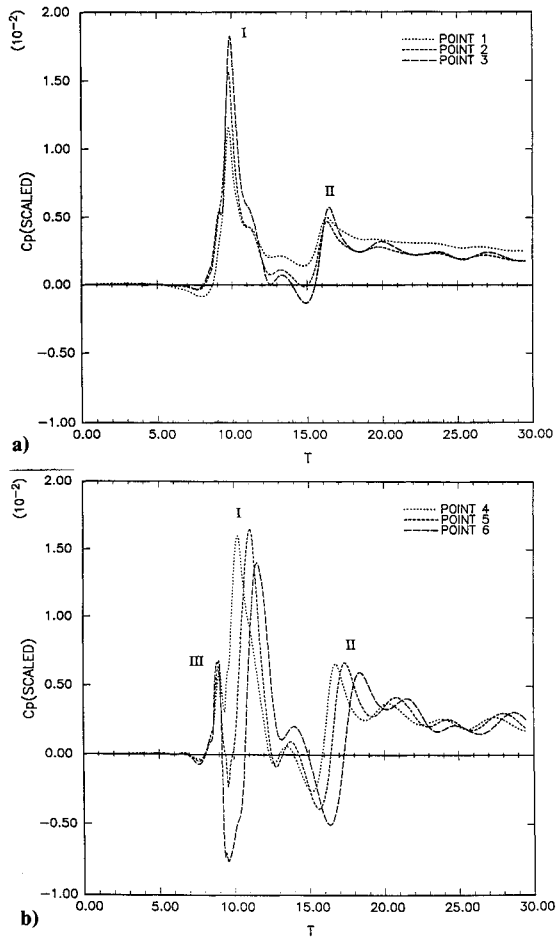

Fig. 7 VTRAN2 $c_p(t)$ results at some points defined in Fig. 5; NACA 64A006, $M = 0.822$, $c_{lv} = 0.4$, $y_o = -0.5$, prescribed vortex path.

where c_o is the speed of sound, U_o is the freestream velocity, subscript 1 implies the acoustic source, and here δ is the well-known Dirac delta function. We should note that Eq. (2) is the same as Eq. (1) without the nonlinear terms. G must satisfy the causality condition for hyperbolic equations

$$G = \frac{\partial G}{\partial t_1} = 0$$

for $t < t_1$.

The solution of Eq. (2) for the subsonic case is given by

$$G = \frac{-\delta(t_1 - t + \tau)}{4\pi r\beta} \tag{3}$$

where

$$r_\beta = \{(x - x_1)^2 + \beta^2[(y - y_1)^2 + (z - z_1)^2]\}^{1/2}$$

$$\tau = [r_\beta - M(x - x_1)]/c_0\beta^2$$

$$\beta = (1 - M^2)^{1/2}$$

This result is well known (see, for example, Morino[19]). If we assume that all the acoustic sources are enclosed by an imaginary closed rigid surface S, then we can prove (Green's theorem) that the pressure distribution outside this surface S is given by

$$p(x,y,z,t) = -\int_{-\infty}^{t-\tau} dt_1 \int_S \left\{ \nabla_1 S\left(G\nabla_1 p - p\nabla_1 G\right) - \left(\frac{1}{c_o^2}\right)\frac{dS}{dt_1}\left[\frac{G\,dp}{dt_1} - \frac{p\,dG}{dt_1}\right]\right\}\frac{dS}{|\nabla_4 S|} \tag{4}$$

where subscript 1 implies the surface S, d/dt_1 is defined as

$$\frac{d}{dt_1} = \frac{\partial}{\partial t_1} + U_o\frac{\partial}{\partial x_1}$$

and $|\nabla_4 S|$ is defined by

$$|\nabla_4 S| = \left[\left(\frac{\partial S}{\partial x}\right)^2 + \left(\frac{\partial S}{\partial y}\right)^2 + \left(\frac{\partial S}{\partial z}\right)^2 + \left(\frac{\partial S}{\partial t}\right)^2\right]^{1/2}$$

If we use the definition of the Green's function given in Eq. (3), then Eq. (4) yields (after some algebra)

$$p = -\frac{1}{4\pi}\iint_{S_\tau}\left\{\frac{1}{r_\beta}\left[\nabla_1 S\cdot\nabla_1 p - \left(\frac{1}{c_o^2}\right)\frac{dS}{dt_1}\frac{dp}{dt_1}\right]_\tau + p_\tau\left[\nabla_1 S\cdot\nabla_1\left(\frac{1}{r_\beta}\right) - \left(\frac{1}{c_o^2}\right)\frac{dS}{dt_1}\cdot\frac{d}{dt_1}\left(\frac{1}{r_\beta}\right)\right]_\tau - \frac{\partial}{\partial t}\left[\nabla_1 S\cdot\nabla_1\tau - \left(\frac{1}{c_o^2}\right)\cdot\frac{dS}{dt_1}\cdot\left(1 + U_o\frac{\partial\tau}{\partial x_1}\right)\right]_\tau\frac{p_\tau}{r_\beta}\right\}\cdot\frac{dS_\tau}{|\nabla_1 S_\tau|} \tag{5}$$

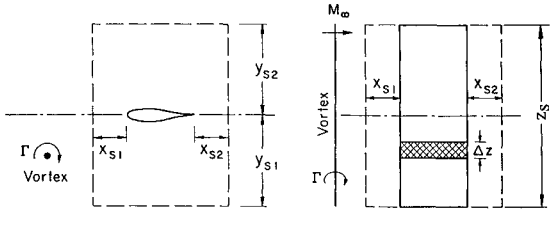

Fig. 8 Side view and top view of the control surface S for the Kirchhoff calculations.

where subscript τ indicates the evaluation at the retarded time $t_1 = t - \tau$.

For a fixed surface ($\partial S/\partial t_1 = 0$), and using the well-known Prandtl-Glauert transformation

$$x_0 = x, \qquad y_0 = \beta y, \qquad z_0 = \beta z, \qquad r_0 = r_\beta$$

we have

$$p = -\frac{1}{4\pi}\int_S\left[\frac{1}{r_0}\cdot\frac{\partial p}{\partial n_0} + \left(\frac{1}{c_o r_o\beta^2}\right)\cdot\frac{\partial p}{\partial t}\cdot\left(\frac{\partial r_o}{\partial n_o} - M\frac{\partial x_{o1}}{\partial n_o}\right) + \left(\frac{p}{r_o^2}\right)\frac{\partial r_o}{\partial n_o}\right]_\tau dS_o \tag{6}$$

where subscript o denotes the transformed values, n is the outward normal to the surface S, and all the values are calculated at the retarded time $t_1 = t - \tau$. The above equations can be also found in Morino,[19,20] and our final Eq. (6) includes one term that was neglected by Morino in his original derivation[19] but was included in later publications (see, for example, Ref. 20).

Thus, the values of the potential and its normal derivatives on an arbitrary surface around the spanwise extent of an arbitrary flow are enough to give the far-field radiation at any arbitrary external point. In our work, we chose to use a rectangular box coinciding with mesh points in order to simplify the computation. The control volume is shown in Fig. 8. The potential and its derivatives can be numerically calculated as before. Since Kirchhoffs method assumes that linear equations hold outside this control surface S, it must be chosen large enough to include the region of nonlinear behavior. However, since the accuracy of the numerical solution is limited to the region immediately surrounding the moving blade, S cannot be so large as to lose accuracy in the numerical solution for the midfield. Thus, a judicious choice of S is required for the effectiveness of this method.

It can be shown that the wake does not need to be included in S, since the pressure is continuous across it. Finally, the distributed vortex, being a region where the homogeneous equation is invalid, should be included within the surface S. However, the effect of including or not including the vortex is comparatively small, particularly as it is nearly unaccelerated while it is outside S. We verified this by trying calculations with surfaces that inlcuded and excluded the vortex when it was near the airfoil.

The y limits of S for our calculations were varied over a range from $y_s = 0.25$ to 4.05 chord lengths distance from the airfoil. If y_s is too small, the vortex and some of the significant nonlinearities are not included and accuracy suffers. On the other hand, if y_s is too large, then the mesh becomes coarser and the accuracy of the input to Kirchhoff's method suffers. The x limits for S were also varied between 0.15-0.50, and values of 0.25 chords upstream and downstream of the leading and trailing edges, respectively, were chosen. A strip-theory approximation was used to look at finite regions of BVI using blade segments ranging from 2 to 16 in aspect ratio. By making calculations with different spans, we found that the tip surface contributions have only a small effect; these were neglected for most of the calculations. The VTRAN2 code is used to calculate the solutions on S.

Moderately close to a high aspect ratio wing, the radiated wave is expected to be two-dimensional ($1/r^{1/2}$ rule), but the far-field is expected to diffract and become three-dimensional ($1/r$ rule). The results for the amplitudes of the perturbation pressure waves of a large number of calculations using both VTRAN2 and the Kirchhoff method are shown in Fig. 9. In the near field, the VTRAN2 calculations initially decay slowly, then decay at a $1/r^{1/2}$ rate in the midfield, and finally decay more rapidly than $1/r^{1/2}$ due to the numerical diffusion and dispersion from the coarse mesh. The Kirchhoff calculations begin two-dimensionally and become three-dimensional ($1/r$

decay) at larger distances. The delineations of the regions depend on the Fraunhofer diffraction parameter $F = \lambda z_s/r^2$, where λ is the wavelength and z_s is the span. For $F \ll 1$ the behavior will be two-dimensional, and for $F \gg 1$ the behavior will be three-dimensional. This behavior is verified by the results shown in Fig. 9.

Midfield and Far-field Results and Discussion

A spherical wave is used first as a test case for the method. A partial sine-wave solution can be defined by the following equation

$$\phi(r,t) = \sin[(t-\tau)\pi/A]/r_\beta$$
$$\text{for } 0 < t-\tau < A \qquad (7)$$

where A is the wave thickness (or half period). The results for this test wave are shown in Fig. 10 for a wave thickness approximately equal to the one expected for a typical BVI. The first curve is the theoretical one, and the second curve is the numerical one found from the Kirchhoff formulation using a mesh that was evenly spaced in each coordinate direction. (However, the mesh spacings in the three directions had different values.) The accuracy of the calculations is seen to be very good. Even for a freestream Mach number of 0.99 (not shown), the results were within 2% of the analytical solution, with very good wave shape. The derivatives on the sides and the ends of the surface S are calculated numerically. Analytical values of the derivatives were also tried without any noticeable improvement.

A base case was selected for the presentation of the results: NACA 64A006, $M = 0.822$, $c_{lv} = 0.4$, $y_o = -0.50$, $y_s = \pm 1.80$, $x_s = \pm 0.25$, $z_s(\text{span}) = 8$, and fixed ($y_v = y_o$, $dx_v/dt = U_o$) path. This case is known[4] to give strong type "C" shock motion. The initial vortex position (in VTRAN2) is -9.51 chords. The normalized freestream velocity is 1, so the vortex arrives below the airfoil at $t = 9.51$.

Figure 11a presents a comparison of the VTRAN2 and the Kirchhoff midfield results at the point no. 5 defined in Fig. 6 for the base case. This point no. 5 is quite close to the surface S used in the Kirchhoff method. The overall comparison is excellent. Parts I and II of the wave are nearly exactly reproduced. Part III is the vortex passage that can be detected in the VTRAN2 solution. In Fig. 11b the Kirchhoff far-field results are shown. The propagation of each of the waves features to the three-dimensional far-field can be seen. We can see, for example, the comparative increase of disturbance II in the far-field, although, of course, the absolute level has decreased.

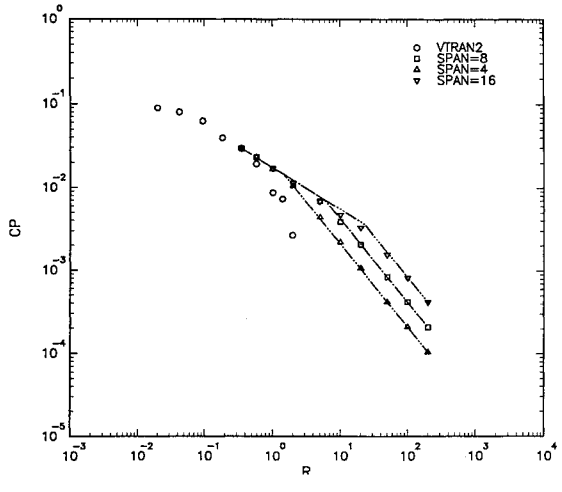

Fig. 9 Log-log plot of wave amplitudes vs r, showing near field $1/r^{1/2}$ and $1/r$ regions for both VTRAN2 and Kirchhoff methods.

Figure 12 indicates the effect of Mach number on the character of the far-field waves. The Mach numbers of 0.875, 0.854, and 0.822 correspond to shock wave motions of types "A", "B", and "C", respectively, where only the type "C" wave escapes from the airfoil and is expected to give the part II of the far-field wave. Indeed, the figure shows this to be the case. The basic disturbance I is slightly increasing with increasing Mach number, while the part II disturbance decreases rapidly with increasing Mach number. The fact that disturbance II does not disappear completely shows that shock

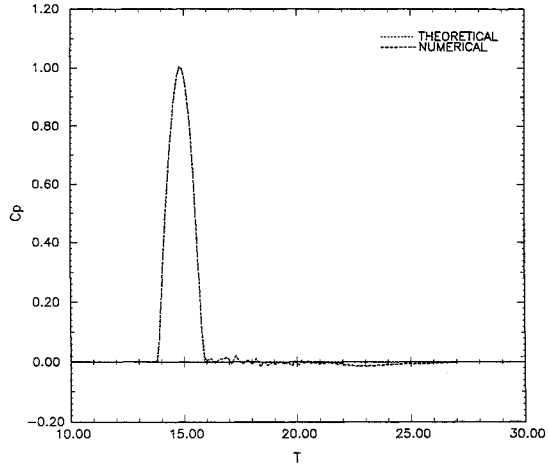

Fig. 10 Results for a spherical wave of sine shape ($x = -3.0$, $M = 0.822$, $A = 0.2$).

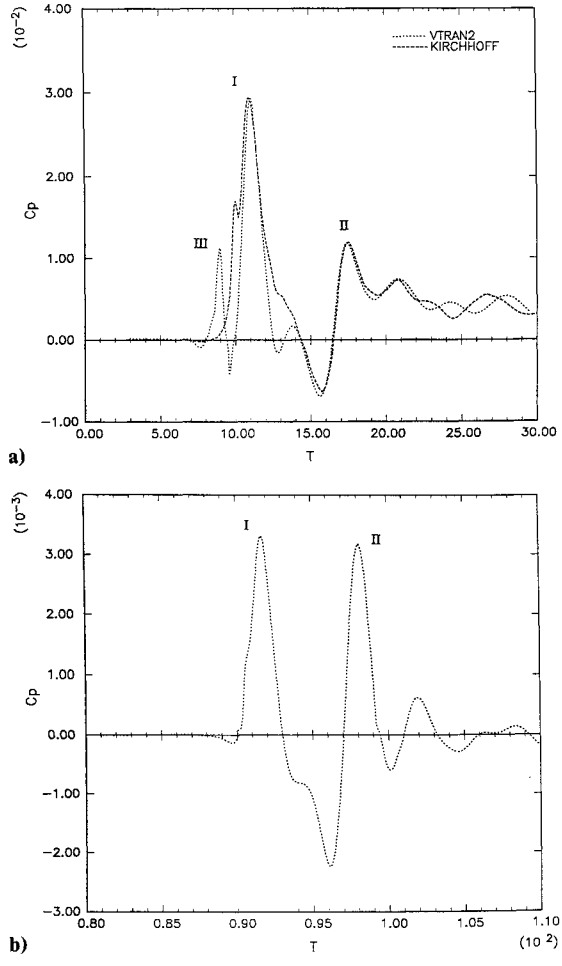

Fig. 11 Base case (except span = 16): Kirchhoff and VTRAN2 results for point no. 5 and Kirchhoff for $r = 20$ far-field.

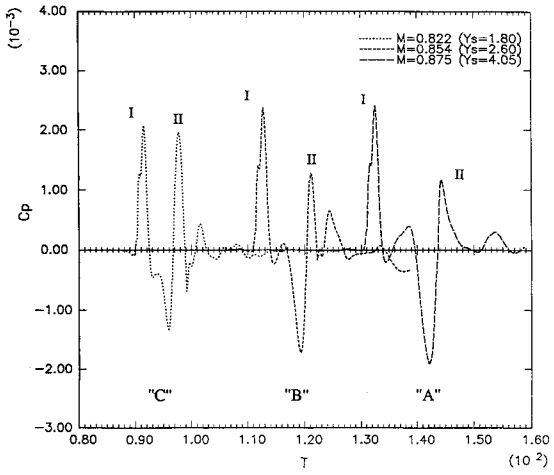

Fig. 12 Effect of Mach number and type of local shock motion on far-field (r = 20); M = 0.875 (type "A"), M = 0.854 (type "B"), and base case M = 0.822 (type "C").

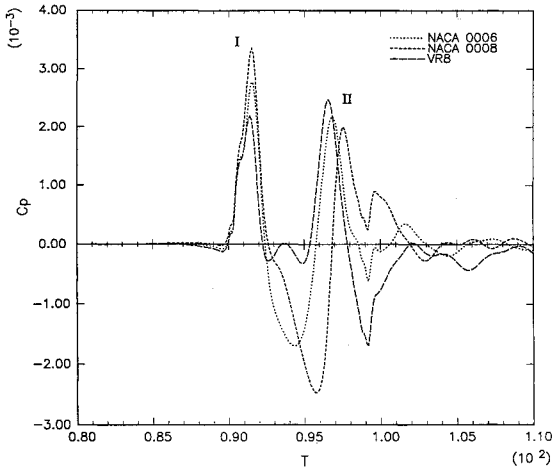

Fig. 14 Effects of airfoil shape and thickness on far-field waves (r = 20); base case NACA 0006 and also 0008 and VR-8.

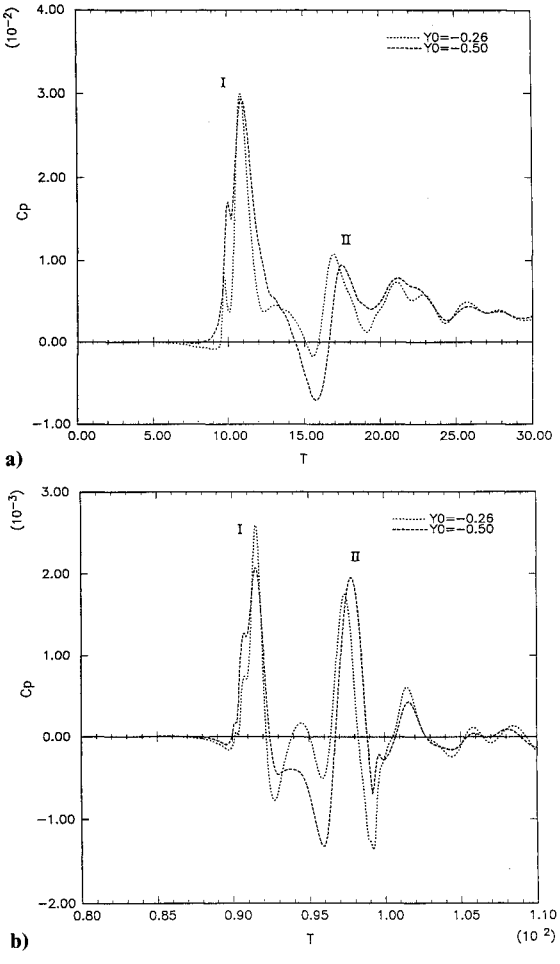

Fig. 13 Effect of vortex initial miss distance below airfoil on midfield (point no. 5) and far-field (r = 20); base case (y_o = −0.50 chords) and y_o = −0.26 chords.

motions type "A" and "B" create some disturbance II signal, although type "C" shock motion creates a much stronger such signal. Also we should note that y_s should be and was increased at higher Mach numbers because of stronger nonlinearities and the larger lateral extent of the disturbed flow region.

The nonlinear effect of vortex miss distance, measured by its initial distance y_o below the airfoil, is shown in Fig. 13. In agreement with the results of Ref. 4, miss distance was found to have a fairly weak effect in the midfield (Fig. 13a), but the effect becomes stronger in the far-field (Fig. 13b). This may be due to the partial focusing (or defocusing) of curved waves in the far-field. The vortex passage near points of observation distorts the resulting waves in the midfield, but in the far-field we can get a more accurate picture. The miss distance has an especially weak effect on the disturbance II, type "C" part of the wave.

Although the results presented in this paper are for prescribed vortex paths, we have obtained results for free vortex paths. The results show that the prescribed path generates a little stronger signal for a prescribed vortex path, as expected. Also some directivity aspects of the far-field noise have been shown and explained in Refs. 9 and 10.

Finally, Fig. 14 shows some of the interesting effects of airfoil shape and thickness. The NACA 0006 airfoil supports a type "C" shock motion. The NACA 0008 airfoil is thicker than the NACA 0006 and supports type "B" shock motion at this Mach number. It has a larger main disturbance I, but a smaller type "C" related disturbance II in the midfield. The more advanced, cambered, small leading-edge radius VR8 airfoil, also of 8% thickness, has a considerably lower disturbance I (even lower than the NACA 0006 disturbance). However, it supports a larger type "C" related disturbance II. The same results were also obtained in the midfield (not shown here). Thus, in this case we see that the maximum thickness of the airfoil and airfoil shape are both important. This fact has also been verified experimentally[17] and computationally[18] by other investigators. We can also deduce that the airfoil shape is more important than the maximum airfoil thickness.

Conclusions

1) A new Kirchhoff method of extending computed two-dimensional midfield results to the three-dimensional far-field has been developed. Good results were obtained on exact linear test cases and in matching Kirchhoff and numerically computed results in their regions of overlapping validity.

2) Explanations were presented for many of the factors relative to the origin of the propagating waves and how well they can be detected in various coordinate systems.

3) It was shown that far-field BVI signatures begin with a primary wave originating in the initial interaction of the blade and vortex. In the case of type "C" shock motion on the blade, an additional important wave is radiated to the far-field at a later time.

4) The far-field radiation is affected by Mach number, airfoil thickness and shape, and vortex miss distance.

Acknowledgments

This research was supported by McDonnell Douglas Helicopter Company. Dr. D.S. JanakiRam was the technical monitor. His encouragement and advice are appreciated by the authors. The authors also acknowledge the contribution of Dr. S.-B. Chang to the testing of the Kirchhoff method for the $M = 0$ case.

This research was conducted on the Cornell University Production Supercomputer Facility of the Center for Theory and Simulation in Science and Engineering, which is funded, in part, by the National Science Foundation, New York State, and IBM Corporation.

References

[1]George, A. R., "Helicopter Noise: State-of-the-Art," *Journal of Aircraft,* Vol. 15, Nov. 1978, pp. 707–715.

[2]Chou, S.-T. and George, A. R., "Helicopter Tail Rotor Noise," AIAA Paper 86-1900, July 1986.

[3]George, A. R. and Chang, S.-B., "Noise Due to Transonic Blade-Vortex Interactions," *Proceedings of the 39th Annual National Forum of the American Helicopter Society,* Washington, DC, Paper A-83-39-50-D000, May 1983.

[4]George, A. R. and Chang, S.-B., "Flow Field and Acoustics of Two-Dimensional Transonic Blade-Vortex Interactions," AIAA Paper 84-2309, Oct. 1984.

[5]Schmitz, F. H. and Yu, Y. H., "Helicopter Impulsive Noise: Theoretical and Experimental Status," *Recent Advances in Aeroacoustics,* edited by A. Krothapalli and C. A. Smith, Springer-Verlag, New York, 1986, pp. 149–243.

[6]McCroskey, W. J. and Goorjian, P. M., "Interactions of Airfoils with Gusts and Concentrated Vortices in Unsteady Transonic Flow," AIAA Paper 83-1691, July 1983.

[7]Srinivasan, G. R., McCroskey, W. J., and Kutler, P., "Numerical Simulation of the Interaction of a Vortex with Stationary Airfoil in Transonic Flow," AIAA Paper 84-0254, Jan. 1984.

[8]Baeder, J. D., McCroskey, W. J., and Srinivasan, G. R., "Acoustic Propagation Using Computational Fluid Dynamics," *Proceedings of the 42nd Annual Forum of the American Helicopter Society,* Vol. 1, Washington, DC, June 1986, pp. 551–562.

[9]George, A. R. and Lyrintzis A. S., "Mid-Field and Far-Field Calculations of Blade-Vortex Interactions," AIAA Paper 86-1854, July 1986.

[10]Lyrintzis, A. S. and George, A. R., "Transonic Blade-Vortex Interactions: The Far-Field," *Proceedings of the American Helicopter Society National Specialists' Meeting on Aerodynamics and Aeroacoustics,* Arlington, TX, Feb. 1987.

[11]Ballhaus, W. F., "Implicit Finite-Difference Computations of Unsteady Transonic Flows about Airfoil," *AIAA Journal,* Vol. 15, Dec. 1977, pp. 1728–1735.

[12]Hessenius, K. A. and Goorjian, P. M., "A Validation of LTRAN2 with High Frequency Extensions by Comparisons with Experimental Measurements of Unsteady Transonic Flows," NASA TM-81307, 1981.

[13]Rizzetta, D. P. and Chin, W. C., "Effect of Frequency in Unsteady Transonic Flow," *AIAA Journal,* Vol. 17, July 1979. pp. 779–781.

[14]Dowling, A. P. and Ffowcs Williams, J. E., *Sound and Sources of Sound,* Ellis Horwood, Chicnester, England, 1983, Chap. 2.

[15]Tijdeman, H., "Investigations of the Transonic Flow Around Oscillating Airfoils," Ph.D. Thesis, Technische Hogeschool, Delft, the Netherlands, 1977.

[16]Tangler, J. L., "Schlieren and Noise Studies of Rotors in Forward Flight," 33rd Annual National Forum of the American Helicopter Society, Washington, DC, Paper 77, 33-05, May 1977.

[17]Caradonna, F. X., Laub, G. H., and Tung C., "An Experimental Investigation of the Parallel Blade-Vortex Interactions," Workshop on Blade-Vortex Interactions, NASA Ames Research Center, Oct. 1984.

[18]Owen, S. T. and Shenoy R. K., "Numerical Investigation of Two-Dimensional Blade-Vortex Interaction," *Proceedings of the American Helicopter Society National Specialists' Meeting on Aerodynamics and Aeroacoustics,* Arlington, TX, Feb. 1987.

[19]Morino, L., "A General Theory of Unsteady Compressible Potential Aerodynamics," NASA CR-2464, Dec. 1974.

[20]Morino, L., "Steady, Oscillatory, and Unsteady Subsonic and Supersonic Aerodynamics—Production Version 1.1 (SOUSSA-P, 1.1), Vol. 1, Theoretical Manual," NASA CR-159130, 1980.